Magnetostructural coupling in ilmenite-type $NiTiO_3$

K. Dey,[1,*] S. Sauerland,[1] B. Ouladdiaf,[2] K. Beauvois,[2] H. Wadepohl,[3] and R. Klingeler[1,4]
[1]*Kirchhoff Institute of Physics, Heidelberg University, INF 227, 69120, Heidelberg, Germany*
[2]*Institut Laue-Langevin, CS20156, 38042 Grenoble Cedex 9, France*
[3]*Institute of Inorganic chemistry, Heidelberg University, 69120, Heidelberg, Germany*
[4]*Center for Advance Materials (CAM), Heidelberg University, INF 227, D-69120, Heidelberg, Germany*

(Received 15 February 2021; accepted 12 April 2021; published 27 April 2021)

We report the ground state magnetic structure and in-field magnetostrictive effects of $NiTiO_3$ studied by means of zero-field and in-field single-crystal neutron diffraction, magnetization, and high-resolution dilatometry experiments. Zero-field neutron diffraction on $NiTiO_3$ single crystals confirms an easy-plane antiferromagnet with a multidomain ground state. Upon application of external magnetic fields, neutron diffraction shows the evolution of domains with spins perpendicular to the applied field. The rotation of spins in the multidomain state exhibits pronounced lattice changes in the magnetostriction measurements. We see magnetization and magnetostriction measurements scale with each other in the multidomain state in accordance with phenomenological theories, revealing the strong coupling of spins to the lattice.

DOI: 10.1103/PhysRevB.103.134438

I. INTRODUCTION

Layered honeycomb magnets have been a great avenue for exciting and rich physics since time immemorial. The recent theoretical and experimental studies of Kitaev quantum spin-liquids in Co-based honeycomb materials [1,2], Dirac magnons [3], and topological spin excitations [4] in honeycomb ferromagnets, nonreciprocal magnons in honeycomb antiferromagnets [5], zigzag [6] and incommensurate [7,8] spin ground states or two-dimensional (2D) magnetism in van der Waals materials [9] have resulted in enormous interest in this class of materials. Moreover, the spin-lattice coupling in several honeycomb magnets such as $Fe_4Nb_2O_9$ [10], $Na_3Ni_2SbO_6$ [11], and $Co_4Nb_2O_9$ [12] has resulted in significant magnetoelectric coupling, hence motivating possible technological applications.

Ilmenite titanates with the chemical formula $MTiO_3$ (M = Mn, Fe, Co, Ni) form an isostructural series of antiferromagnetic (AFM) compounds where magnetic M^{2+} ions in the basal ab plane exhibit a buckled honeycomblike structure. The M^{2+} ions are interconnected via oxygen ions (O^{2-}), leading to M-O-M as the dominant superexchange pathway [13]. Along the c axis, the crystal structure exhibits alternating layers of corner-sharing TiO_6 and MO_6 octahedra, resulting in relatively weaker M-O-Ti-O-M superexchange pathways. Depending on the single ion anisotropies of the respective metal ions, various magnetic ground states are realized in ilmenites, for example, uniaxial AFM ground state with spins pointing along the c axis in $MnTiO_3$ [14] or an easy-plane-type AFM with spins lying in the ab plane for $NiTiO_3$ and $CoTiO_3$ [15], respectively.

Although these compounds have been rigorously investigated [13,14,16–18], recent studies evidencing linear magnetoelectric coupling in $MnTiO_3$ [19], large spontaneous magnetostriction in $FeTiO_3$ [20], magnetodielectric and magnetoelastic coupling in $NiTiO_3$ [21,22] and $CoTiO_3$ [23], respectively, as well as the observance of Dirac magnons in $CoTiO_3$ [24,25] have piqued enormous interest in this class of materials.

The least investigated compound among the ilmenites family, i.e., $NiTiO_3$, develops long-range AFM order at T_N = 22.5 K [16,21,22,26]. Recent studies of the dielectric permittivity and the thermal expansion show a pronounced magnetodielectric effect [21] as well as distinct significant magnetoelastic coupling [22]. Notably, at T_N, there is a single dominant energy scale driving the observed structural, magnetic, and dielectric anomalies [22]. In this paper, we study in detail the magnetostructural coupling of $NiTiO_3$ by means of single-crystal x-ray and neutron diffraction and high-resolution dilatometry. We observe by means of single-crystal neutron diffraction that the macroscopic structural symmetry (R-3) is retained down to the lowest measured temperature of 2 K within the experimental resolution. In addition, the magnetic ground state of $NiTiO_3$ is solved. At T_N, in addition to long-range AFM order, a significant lattice distortion evolves, revealing large spontaneous magnetostriction in $NiTiO_3$. In applied magnetic fields, the multidomain ground state evolves to a spin-reoriented single domain state characterized by spins aligned perpendicular to the applied magnetic field. Magnetostriction measurements in the low-field region show pronounced effects due to magnetoelastic domains and remarkably scale with magnetization measurements, confirming both significant magnetostructural coupling and the magnetostructural domain model in $NiTiO_3$.

II. EXPERIMENTAL METHODS

Macroscopic single crystals of $NiTiO_3$ were grown by means of the optical floating-zone technique in a four-mirror

*kaustav.dey@kip.uni-heidelberg.de

optical floating-zone furnace (CSC, Japan) equipped with 4×150 W halogen lamps. Details of the growth process and characterization the single crystals have been published previously [22]. Single-crystal x-ray intensity data were obtained at 100 K with an Agilent Technologies Supernova-E CCD 4-circle diffractometer (Mo-Kα radiation $\lambda = 0.71073$ Å, microfocus x-ray tube, multilayer mirror optics). Static magnetization $\chi = M/B$ was studied in magnetic fields up to 5 T in a Quantum Design MPMS-XL5 SQUID magnetometer. The relative length changes dL_i/L_i were studied on a cuboid-shaped single crystal of dimensions $2 \times 1.85 \times 1$ mm^3 by means of a three-terminal high-resolution capacitance dilatometer [11,27]. Magnetostriction, i.e., field-induced length changes $dL_i(B)/L_i$, was measured at several fixed temperatures in magnetic fields up to 15 T, and the longitudinal magnetostriction coefficient $\lambda_i = 1/L_i dL_i(B)/dB$ was derived. The magnetic field was applied along the direction of the measured length changes.

Single-crystal neutron diffraction experiments were performed up to 6 T magnetic fields at the D10 beamline of the Institut Laue-Langevin (ILL) at Grenoble, France. To determine the magnetic ground state at $B = 0$ T, the four-circle configuration was used with a 96×96 mm^2 2D microstrip detector. An incident wavelength of 2.36 Å using a vertically focusing pyrolytic graphite (PG) (002) monochromator was employed. A PG filter was used to suppress higher-order contamination to 10^{-4} times that of the primary beam intensity. Measurements were made in the temperature range 2–50 K. The magnetic field-driven evolution of the magnetic structure at $T = 2$ K was studied by mounting the sample in a 6 T vertical cryomagnet and aligned to within 1° of magnetic field. The magnetic field was applied along the b axis, limiting the scattering to the $(H, 0, L)$ plane.

III. EXPERIMENTAL RESULTS

A. Single-crystal x-ray diffraction

To the best of our knowledge, the earlier studies of the ilmenite-type $NiTiO_3$ crystal structure have been limited to powder diffraction experiments only [14,22,28]. We have reinvestigated the crystal structure by means of single-crystal high-resolution x-ray diffraction (XRD) at 100 K, using Mo-Kα radiation ($\lambda = 0.71073$ Å). A single-crystal splinter of size $0.16 \times 0.14 \times 0.01$ mm^3 was broken off from a larger specimen and used for data collection. A full shell of intensity data was collected up to 0.4 Å resolution {24 180 reflections, 1028 independent ($R_{\text{int}} = 0.05$) of which 1024 were observed [$I > 2\sigma(I)$]}. Detector frames (typically ω, occasionally ϕ scans, scan width 0.5°) were integrated by profile fitting [29]. Data were corrected for air and detector absorption, Lorentz and polarization effects [30], and scaled essentially by application of appropriate spherical harmonic functions [30–32]. Absorption by the crystal was treated numerically (Gaussian grid) [32,33]. An illumination correction was performed as part of the numerical absorption correction [32]. Space group R-3 was assigned based on systematic absences and intensity statistics (refined obverse centered unit cell on hexagonal axes, Hall group $-R3$, $a = 5.02762(6)$, $c = 13.76711(17)$ Å, $V = 301.369(8)$ Å^3, and $Z = 6$). This choice was confirmed by analysis of the symmetry of the phases obtained *ab initio* in P1. The structure was solved by intrinsic phasing [34–36] and refined by full-matrix least-squares methods based on F^2 against all unique reflections [37–40]. Three somewhat different models were employed for the atomic structure factors f_{at} within the independent spherical atoms approximation: conventional f_{at} calculated with neutral atoms [41] for Ni, Ti, and O (model A) and two "ionic" models [41] {f_{at} for Ni^{2+} and Ti^{4+} taken from Ref. [41] and O^{2-} from Ref. [42] (model B) or Ref. [43], respectively (model C)}. An empirical secondary extinction correction [38,44] was applied in each case but proved insignificant. The different models refined to essentially the same structure, with only insignificant differences in key parameters like atom coordinates, R factors, U_{eq} for all atoms, and residual electron density. Ni-O and Ti-O bond lengths agreed within one standard deviation. There was no evidence of cation mixing, and fully occupied sites were employed for all atoms. The results confirm the assignment of the space group and improve on the accuracy of the crystallographic parameters previously obtained from powder XRD and neutron data [14,22,28]. Fractional atomic coordinates, Wyckoff positions, site occupation, and equivalent isotropic displacement parameters for model A are listed in Table I [45].

TABLE I. Fractional atomic coordinates, Wyckoff positions, site occupation, and equivalent isotropic displacement parameters (Å^2) for $NiTiO_3$ at 100 K, as obtained from refinement of model A. (Note: (1) These coordinates are correct but do not form a uniquely bonded set; (2) U_{eq} is defined as one-third of the trace of the orthogonalized U_{ij} tensor. The anisotropic displacement factor exponent takes the form $-2\pi^2[h^2a^{*2}U_{11} + ... + 2hka^*b^*U_{12}]$).

Atom	Site	x	y	z	sof	U_{eq}
Ni	6c	0	0	0.35051 (2)	1	0.00308 (2)
Ti	6c	0	0	0.14422 (2)	1	0.00297 (3)
O	18f	0.35198 (8)	0.03455 (8)	0.08662 (2)	1	0.00421 (4)

B. Single-crystal neutron diffraction

The crystal structure at lower temperatures and the magnetic ground state of $NiTiO_3$ were determined by means of single-crystal neutron diffraction. At 50 K, 110 nuclear Bragg reflections were collected. Appropriate correction for extinction, absorption, and Lorentz factor was applied to all the nuclear Bragg peaks. All the nuclear peaks at 50 K were successfully indexed in the R-3 space group with lattice parameters $a = 5.03$ Å and $c = 13.789$ Å.

To clarify the magnetic structure, preliminary reciprocal-space scans (not shown here) were performed at 2 K along the $(0, 0, L)$, $(H, 0, 0)$, and $(H, K, 0)$ directions. The scans reveal a peak of significant intensity emerging at (0,0,1.5), indicative of the propagation vector $\mathbf{k} = (0,0,1.5)$. To determine the detailed magnetic structure, integrated intensities of 187 nuclear reflections allowed within the space group R-3 and 292 satellite magnetic reflections were collected at 2 K. The nuclear structure was firstly refined using FULLPROF program within the R-3 space group. The results of refinement are listed in Table II, and the observed and calculated intensities from the Rietveld fits are shown in Fig. 2(a). No peak splitting or

TABLE II. Parameters for the nuclear structure of $NiTiO_3$ measured at 2 K obtained from refinements of single-crystal neutron diffraction data. The isotropic temperature factors (B_{iso}) of all atoms were refined. [Space group: R-3 (148); Lattice parameters: $a = b = 5.0229(1)$ Å, $c = 13.7720(1)$ Å, $\alpha = \beta = 90°$, and $\gamma = 120°$.]

Atom	Site	x	y	z	B_{iso}(Å^2)
Ni1	6c	0	0	0.3537 (2)	0.00748
Ti1	6c	0	0	0.1338 (5)	0.06643
O1	18f	0.3344 (6)	0.0052 (1)	0.2466 (2)	0.09830

significant broadening was observed within the experimental resolution in respective 2 K nuclear reflections as compared with 50 K, indicating that the macroscopic R-3 symmetry is maintained until the lowest measured temperatures. The nuclear Bragg peaks show no temperature dependence between 2 and 50 K excluding $\mathbf{k} = (0,0,0)$.

All the finite intensity magnetic peaks are observed at the general position $(H, K, L) + (0,0,1.5)$ with H, K, L satisfying the reflection conditions of the R-3 space group and hence confirming $\mathbf{k} = (0,0,1.5)$. A few of the observed high-intensity magnetic peaks are listed in Table III. The largest diffraction intensity occurs for the magnetic Bragg peak (0,0,1.5), indicating that the Ni^{2+} moments lie in the ab plane, which had been suggested by previous magnetization measurements [22]. The temperature dependence of the integrated intensity of the commensurate reflection (0,0,1.5) in Fig. 1 shows finite intensity below the magnetic ordering temperature. A power law fit in the critical region using $I \propto M^2 \propto \tau^{2\beta}$, where M is the order parameter and $\tau = 1 - T/T_N$ results in $T_N = 22$ (1) K and $\beta = 0.35(1)$. The obtained value T_N from the power law fit agrees to the one from previous macroscopic studies [16,21,22,26]. The obtained value of the critical parameter $\beta = 0.35(1)$ lies in between the three-dimensional (3D) XY ($\beta = 0.345$) and 3D Heisenberg ($\beta = 0.367$) universality classes. However, the previously reported pulsed-field M vs B measurements revealed an isotropic behavior for $B||ab$ and $B||c$ [22], indicating that Ni^{2+} spins in $NiTiO_3$ are of 3D Heisenberg nature.

The knowledge of the propagation vector $\mathbf{k} = (0,0,1.5)$ with the Ni^{2+} moments lying in the hexagonal ab plane points

TABLE III. Observed intensities (I_{obs}) of several high-intensity magnetic peaks, as measured in D10 at 2 K and their corresponding calculated intensities (I_{cal}), as discussed in the text.

Q	I_{obs}	I_{cal}
(0,2,2.5)	975 (17)	917
(0,2,5.5)	1410 (27)	1307
(0,−1,5.5)	2481 (36)	2685
(0,0,4.5)	2809 (22)	3348
(1,−2,−1.5)	1923 (20)	2045
(1,−2,4.5)	1755 (22)	1521
(0,−1,2.5)	1787 (17)	1965
(−1,2,4.5)	1812 (48)	1521
(0,−1,8.5)	1729 (109)	1679
(0,0,1.5)	4366 (21)	3942

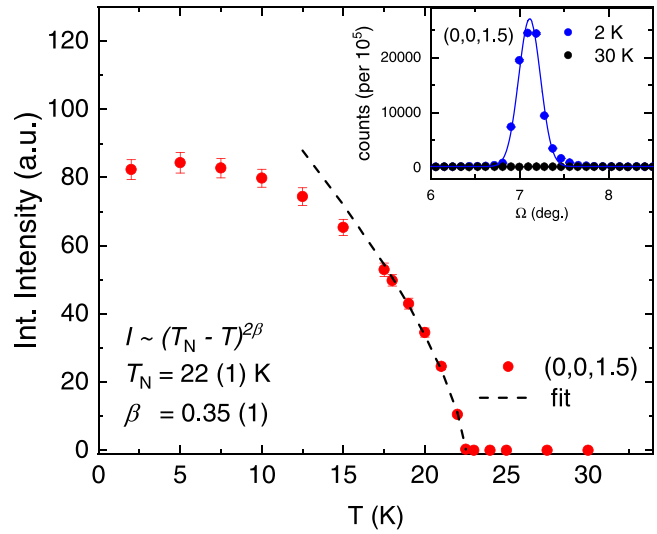

FIG. 1. Temperature dependence of the integrated intensity of the (0,0,1.5) magnetic Bragg peak. The dashed black curve is a fit to the data with the power law $I \sim (T_N - T)^{2\beta}$. The inset shows the Ω scan through the magnetic (0,0,1.5) peak at 2 and 30 K, respectively. The solid blue line is the Gaussian fit to the peak at 2 K. See the text for more details.

toward two possible magnetic models for $NiTiO_3$: (a) ferromagnetic layers stacked AFM along the c axis or (b) AFM layers with the spins aligned ferromagnetically along the c axis. Previous static magnetic susceptibility $\chi = M/H$ vs T measurements reveal the decrease of χ_{ab} below T_N, whereas χ_c stays nearly constant [22,26]. Moreover, the magnetic model (b) implies a zero magnetic structure factor at the position $Q = (0, 0, 1.5)$, contrary to our observation. Hence, model (a) is most suitable to describe the magnetic structure of $NiTiO_3$. The obtained magnetic peaks at 2 K were refined against model (a), and a very good fit was obtained, as shown in Fig. 4(b). The obtained magnetic structure of $NiTiO_3$ reconfirms the structure proposed by Shirane *et al.* [14] based

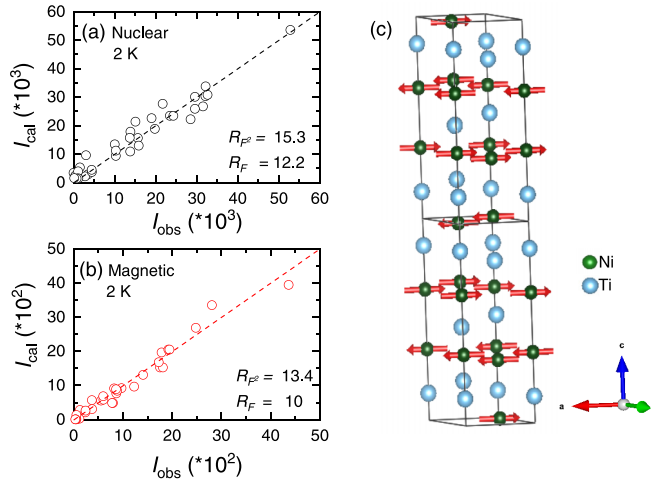

FIG. 2. Comparison between the observed and calculated integrated intensities of the nonequivalent (a) nuclear and (b) magnetic reflections, respectively, at 2 K, and (c) easy-plane-type magnetic structure of $NiTiO_3$, as determined from the refinements at 2 K.

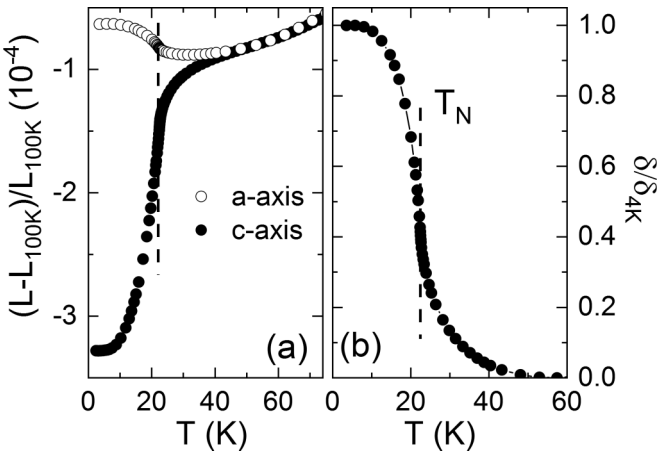

FIG. 3. (a) Relative length changes $dL_i^* = (L_i - L_i^{100\,\mathrm{K}})/L_i^{100\,\mathrm{K}}$ measured along the principle crystallographic a and c axes, respectively, by means of high-resolution dilatometry. (b) Normalized distortion parameter $\delta/\delta_{4\,\mathrm{K}}$, with $\delta = (dL_a^* - dL_c^*)/(dL_a^* + dL_c^*)$. The vertical dashed lines indicate T_N.

on powder neutron data . The observed and calculated intensities of several magnetic peaks are listed in Table III, and the complete magnetic structure of $NiTiO_3$ is schematically represented in Fig. 2(c). At $T = 2$ K, the ordered moment amounts to 1.46 (1) μ_B.

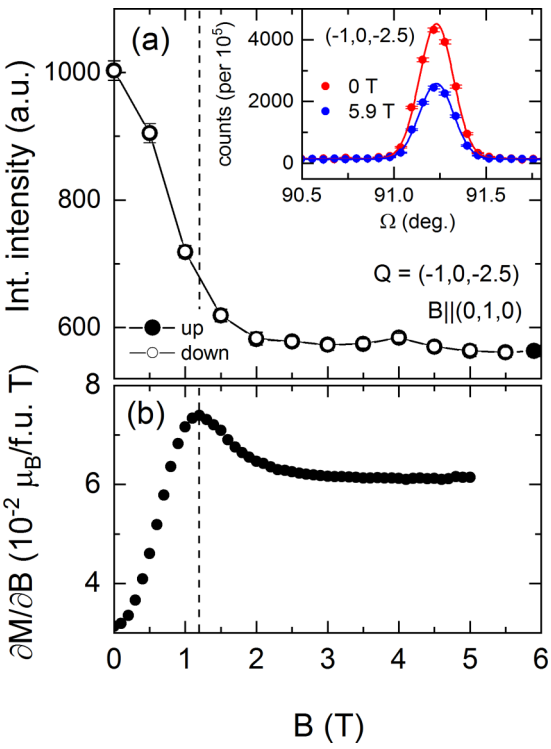

FIG. 4. (a) Integrated intensity of the magnetic (−1,0,−2.5) peak as a function of magnetic field (up and down) and (b) the derivative of static magnetization with respect to magnetic field $\partial M/\partial B$ as a function of magnetic field (from Ref. [22]) at 2 K. The inset to (a) shows the Ω scans through the magnetic (−1,0,−2.5) peak at 0 and 5.9 T. The solid lines in blue and red are Gaussian fits to the peaks at 0 and 5.9 T, respectively.

The crystal symmetry of the basal hexagonal planes is marked by the presence of two sets of three twofold axes. Hence, the in-plane spin configurations rotated by 120° are exactly equivalent, leading to the presence of spin domains (i.e., three domains). Since the refinements are usually performed using the average of the integrated intensities of the equivalent reflections, the directions of the spins cannot be uniquely determined using single-crystal neutron diffraction alone, like the problem existing in the earlier powder diffraction experiments [14]. However, excellent agreement of the integrated intensities between the equivalent reflections ($R_\mathrm{int} = 1.86\%$ indicates that there are likely three spin domains of equal population with spins rotated by 120° in between the neighboring domains.

C. Magnetostructural-dielectric coupling

The magnetostructural coupling in $NiTiO_3$ has been studied by means of high-resolution capacitance dilatometry. The uniaxial relative length changes $dL_i^* = (L_i - L_i^{100\,\mathrm{K}})/L_i^{100\,\mathrm{K}}$ ($i = a, c$) [Fig. 3(a)] vs temperature show abrupt changes at T_N, i.e., shrinking of the c axis and expansion along the a axis, which demonstrates significant magnetoelastic coupling in $NiTiO_3$. At higher temperatures $T \geqslant 50$ K, isotropic thermal expansion coefficients result in similar rate of increase of dL_i^* along the a and the c axes, respectively. To further elucidate lattice changes at T_N, the normalized distortion parameter $\delta/\delta_{4\mathrm{K}}$, with $\delta = (dL_a^* - dL_c^*)/(dL_a^* + dL_c^*)$, is shown in Fig. 3(b).

As evidenced by the distortion parameter, different behavior of the a and c axes starts to evolve gradually below 50 K, while δ sharply jumps at T_N [Fig. 3(a)]. Evidently, the onset of long-range AFM order is associated with a large spontaneous magnetostriction effect, and it implies strong magnetostructural coupling. Spontaneous magnetostriction has also been observed in other ilmenites such as $FeTiO_3$, which however shows a reversed magnetostrictive effect, i.e., expansion of the c axis and shrinking of the a axis [20]. We attribute this difference to the differing magnetic ground states in $FeTiO_3$ and $NiTiO_3$ and corresponding variation in magnetocrystalline anisotropy. Finite distortion δ up to 50 K evidences a precursor phase with short-range order well above T_N. Due to the observed strong magnetoelastic coupling, we conclude the presence of short-ranged spin correlations persisting up to twice the transition temperature. This is corroborated by previous specific heat measurements [22] on $NiTiO_3$, which reveal that nearly 20% of magnetic entropy is consumed between T_N and 50 K. In addition, it has been shown that the **q**-dependent spin-spin correlations couple to the dielectric response via the coupling of magnetic fluctuations to optical phonons, thereby causing a significant magnetocapacitance effect [46]. Accordingly, we conclude that the significant magnetocapacitance of 0.01% and finite magnetostriction recently observed in $NiTiO_3$ well above T_N is due to persisting spin-spin correlations [21,22].

D. Spin reorientation

The effect of magnetic fields applied within the *ab* plane on the crystal and magnetic structure of $NiTiO_3$ is studied by

means of in-field neutron diffraction at 2 K. Specifically, the magnetic field is applied vertically along the b axis, and the scattering vector lies in the $(H, 0, L)$ plane. Several nuclear and magnetic reflections were measured with rocking curve scans in magnetic fields up to 6 T. As will be discussed below, there is a considerable decrease in intensity upon application of the magnetic field for all magnetic peaks, while in contrast, there is no magnetic field effect on the nuclear peak intensities. A representative scan through the magnetic peak $Q = (-1,0,-2.5)$ is shown in the inset to Fig. 4.

The magnetization curve displays a nonlinear dependence on magnetic fields applied along the ab plane, as evidenced by the magnetic susceptibility $\chi = \partial M/\partial B$ in Fig. 4(b). The maximum in χ at $B = 1.2$ T is indicative of a spin-reorientation transition. Correspondingly, the integrated magnetic intensity [Fig. 4(a)] shows a continuous decrease in magnetic fields up to 2 T, above which it stays nearly constant at a finite value. Since the magnetic neutron diffraction intensity is proportional to the component of the magnetic moments perpendicular to the scattering vector, this observation indicates that, in magnetic field, the spins are rotated smoothly from three magnetic domains to a single domain state with spins aligned perpendicular to fields >2 T. Between 2 and 6 T, negligible field dependence indicates a very small canting of spins toward the magnetic field. The full width at half maximum calculated using Gaussian fits to nuclear peaks show negligible broadening up to 6 T, indicating that the magnetostriction effects on lattice parameters corresponding to the spin reorientation are below the experimental resolution.

E. Magnetostriction

Applying magnetic fields along the ab plane yields a pronounced increase of the associated lattice parameter in the low-field region ($B < B^* = 2$ T), while there is only small magnetostriction at higher fields (see Fig. 5). Magnetostriction is also reportedly small for fields applied along the c axis [22]. We conclude that this behavior is associated with the field-driven collective rotation of spins, as discussed above and evidenced by Fig. 4. However, as will be discussed below, the magnetization changes do not scale with magnetostriction, and the maxima in $\partial M/\partial B$ and $\partial L_a/\partial B$ do not match each other [see Fig. 8(a)]. The magnetostriction data hence do not correspond to what is expected for a thermodynamic spin-reorientation transition. Instead, the presence of domains has to be involved, and in the following, we will present clear evidence that the data represent the change from a low-field multidomain state to a high-field uniform monodomain one.

To further investigate the effect of in-plane magnetic fields, the intensity evolution of two equivalent magnetic Bragg peaks (3,0,1.5) and (−3,0,−1.5) belonging to two different magnetic domains is displayed in Fig. 5(c). In the multidomain state, the AFM vector is uniform within a single domain and has different directions in different domains. The observed isotropic decrease in intensity of both magnetic peaks upon application of the magnetic field implies that the spins of both domains rotate perpendicularly to the external field direction. The spin-rotation process is completed at 2 T, which hence signals the formation of a spin-reoriented monodomain state. Accordingly, no significant changes in the peak intensities are observed between 2 and 6 T.

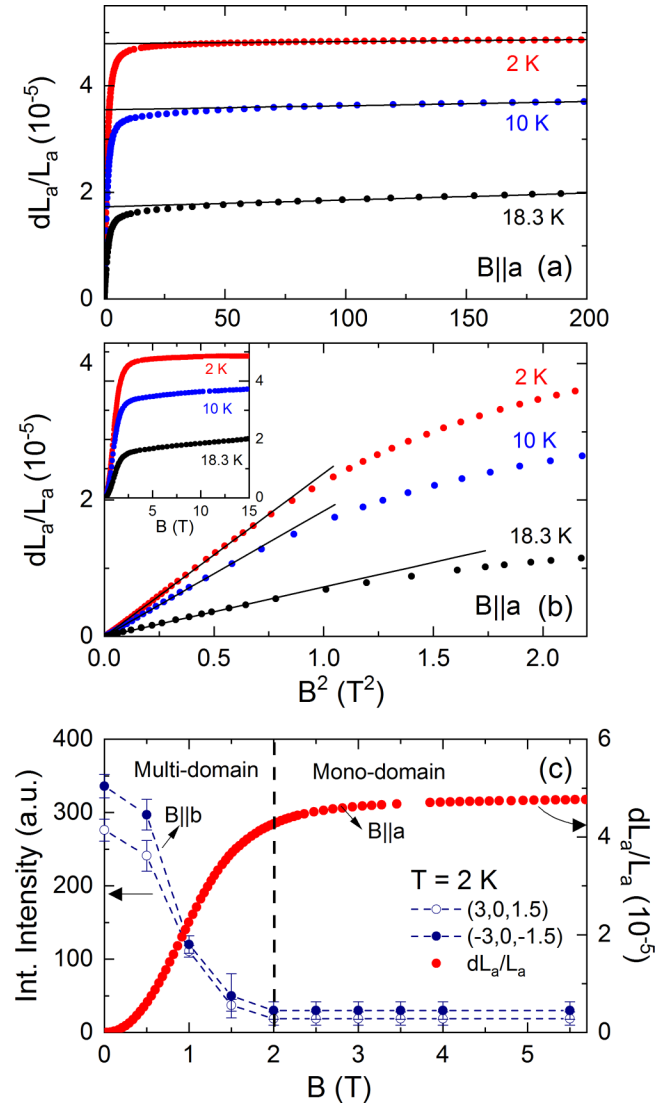

FIG. 5. Relative length changes dL_a/L_a at different temperatures vs the square of magnetic field applied along the crystallographic a axis for (a) magnetic fields up to 14 T, i.e., including the high-field single-domain (homogeneous) phase, and (b) for $B \leqslant 1.5$ T, which is the low-field multidomain phase (see the text). The solid black lines are corresponding linear fits. The inset to (b) shows the relative length changes vs applied magnetic field. (c) Integrated intensity of the equivalent magnetic Bragg peaks (3,0,1.5) and (−3,0,−1.5) vs magnetic field applied along the b axis and (dL_a/L_a) for fields along a axis, at $T = 2$ K. The vertical dashed line separates the multidomain and the monodomain (homogeneous) regions. See text for more details.

IV. DISCUSSION

Comparison of the magnetic order parameter and the relative volume changes with the reported data of the dielectric function by Harada *et al.* [21] elucidates the coupling mechanism between the lattice and the dielectric degrees of freedom in $NiTiO_3$. As displayed in Fig. 6(a), the nonphononic relative volume changes $dV'/V = 2(dL_a/L_a) + (dL_c/L_c)$ which are obtained by subtracting the phononic contribution from dV/V (cf., Ref. [22]) show a very similar temperature dependence, below T_N, as the normalized dielectric permittivity. Note that

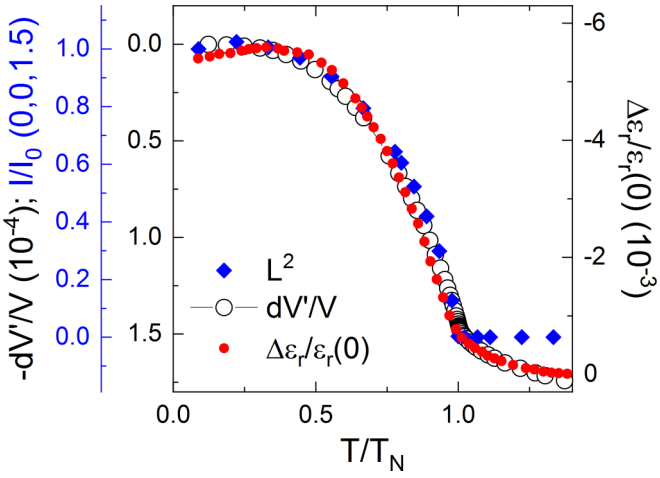

FIG. 6. Temperature dependence of the square of the antiferromagnetic order parameter (L^2), i.e., the normalized integrated intensity of the (0,0,1.5) magnetic Bragg peak, the negative nonphononic volume changes dV'/V, and the normalized dielectric permittivity digitized from Ref. [21].

the polycrystalline sample studied in Ref. [21] displays a slightly lower T_N than the single crystals studied at hand. In general, the length changes can directly affect the experimentally measured permittivity via the relation $\epsilon = Cd/\epsilon_0 A$, where C, ϵ_0, d, and A are sample capacitance, vacuum permittivity, sample thickness, and area, respectively. However, the changes in sample dimensions at T_N are on the order of 10^{-4}, while the relative change in permittivity is an order higher, implying that spontaneous magnetostriction is not the driving mechanism for the observed dielectric changes at T_N. Interestingly, the normalized dielectric permittivity varies as the square of the AFM order parameter L, represented by the normalized integrated intensity of the magnetic (0,0,1.5) Bragg peak in Fig. 6(a). To discuss this, we recall the Landau expansion of the free energy F, in terms of polarization P, and the sublattice magnetization L at zero magnetic field [47]:

$$F = F_0 + \alpha P^2 + \alpha' L^2 + \beta PL + \gamma P^2 L^2 - PE, \qquad (1)$$

The dielectric function is obtained as $\partial^2 F/\partial P^2 = \epsilon \propto \gamma L^2$. Hence, Fig. 6(a) qualitatively evidences the presence of magnetodielectric coupling in $NiTiO_3$. On top of the spin and dielectric changes, the structural changes exhibit similar behavior below T_N. Previously reported magnetic Grüneisen analysis [22] evidences that the entropic changes at T_N are of purely magnetic nature. In our opinion, the spin-phonon coupling is responsible for observed dielectric changes at T_N. In the presence of spin-phonon coupling, the phonon frequency ω can be affected by spin correlation as $\omega = \omega_0 + \lambda\langle S_i.S_j\rangle$, resulting in modification of permittivity via the Lyddane–Sachs–Teller equation $\epsilon_0 = {\omega_L}^2/{\omega_T}^2\epsilon_\infty$, where ϵ_0 and ϵ_∞ are the permittivity at zero frequency and optical frequency, respectively, and ${\omega_L}^2$ and ${\omega_T}^2$ are the long-wavelength longitudinal and transverse optical phonon modes, respectively.

It is noteworthy that, apart from spontaneous magnetostriction, an exchange-striction (ES) mechanism may in principle also lead to spontaneous lattice deformation at T_N and be a potential source for dielectric anomaly at T_N. Magnetodielectricity fueled by an ES mechanism have been observed in several systems, for example, $Y_2Cu_2O_5$ [48] and $TeCuO_3$ [46]. In $FeTiO_3$, a combination of ES and magnetostriction mechanisms have been suggested for the spontaneous lattice deformation at T_N [20]. For $NiTiO_3$, an ES mechanism would imply a change in the Ni-O-Ni bond angle in the *ab* plane closer to 90°, favoring ferromagnetic superexchange. However, diffraction experiments reveal that the bond angle increases from 90.34° at 100 K to 90.36° at 2 K (Supplemental Material, Fig. 2 [49]), contrary to predictions of ES. Hence, an ES mechanism is excluded as the origin of lattice distortion at T_N in $NiTiO_3$.

The crystallographic symmetry of the easy hexagonal plane in $NiTiO_3$ suggests the presence of three domains with spins rotated by 120° in different domains. Such a spin structure with three domains is often observed in easy-plane-type hexagonal antiferromagnets such as $CoCl_2$, $NiCl_2$, and $BaNi_2V_2O_8$ [50,51]. In $NiTiO_3$, the magnetostriction data imply that the field-driven changes of the domain structure is associated with structural changes. Indeed, orientational AFM domains are magnetoelastic in nature [52,53] and have previously been observed in various systems, for example, in cubic antiferromagnets $RbMnF_3$ [54], $KNiF_3$ and $KCoF_3$ [55,56], NiO [57], iron-group dihalides $CoCl_2$ [58] and $NiCl_2$ [59], the quasi-2D AFM $BaNi_2V_2O_8$ [51], $YBa_2Cu_3O_{6.3}$ [53], etc. Kalita *et al.* [58–62] have developed phenomenological theories describing the effect of domain redistribution on the magnetostriction for $CoCl_2$ and $NiCl_2$. Note that both $NiCl_2$ and $CoCl_2$ are easy-plane-type antiferromagnets with similar crystalline symmetry, i.e., trigonally distorted octahedral environment surrounding metal ions, like $NiTiO_3$ and $CoTiO_3$ [50,63]. In the following, we will describe the field dependency of the length changes in $NiTiO_3$ based on the phenomenological theories developed by Kalita *et al.* [58–62].

Both at low magnetic fields $B||a \leqslant 1$ T and at higher fields, the field-induced striction dL_a/L_a varies as the square of the applied magnetic field, as shown in Figs. 5(a) and 5(b). In the latter, i.e., the monodomain state, this is predicted by calculating the equilibrium elastic strain by energy minimization of the magnetoelastic and the elastic contributions to the free energy [58,59]. The magnetostriction in the monodomain state is described by

$$\left(\frac{dL_a}{L_a}\right)(T,B) = \alpha(T)B^2 + \left(\frac{dL_a}{L_a}\right)_s(T, B=0), \qquad (2)$$

where $\alpha(T)$ is the temperature-dependent slope, and $(dL_a/L_a)_s(T, H=0)$ is the spontaneous magnetostriction of the monodomain state obtained by extrapolating the linear fit to $B = 0$ T. Equation (2) fits well with dL_a/L_a at different temperatures, as shown by the solid black lines in Fig. 5(a). The obtained fit parameters are listed in Table IV. Here, $(dL_a/L_a)_s$ corresponds with a hypothetical spontaneous striction that would be observed if the magnetoelastic domains did not appear at low fields, i.e., if the total spontaneous magnetostriction was not compensated on the whole by summation of strains in different directions in each of the domains.

The magnetostrictive response upon application of magnetic fields in the multidomain state is governed by

TABLE IV. Parameters obtained from fits to the magnetostriction data [Figs. 5(a) and 5(b)] using Eqs. (2) and (3). $(dL_a/L_a)_s$ is the spontaneous magnetostriction (see the text).

T	$(dL_a/L_a)_s(10^{-5})$	B_d (T)	α (10^{-9}) (T^2)
2 K	4.79	1.41	3.8
10 K	3.55	1.38	7.6
18.3 K	1.73	1.55	12.8

domain-wall motion. Specifically, magnetostriction is large due to the associated facilitated rotation of spins. The motion of magnetoelastic domain walls is predominantly reversible in nature [52,55], and the associated length changes again exhibit a square dependence on the magnetic field, which is expressed by

$$\left(\frac{dL_a}{L_a}\right)(T,B) = \left(\frac{dL_a}{L_a}\right)_s (T, B=0) \times \left(\frac{B}{B_d}\right)^2. \quad (3)$$

Here, H_d is an empirical parameter obtained from the fits (see Table IV). As shown in Fig. 5(b), the experimental data are well described by Eq. (3), which is in line with the predictions of phenomenological models [55,59]. Although the magnetoelastic domains are predominately reversible in nature, a small irreversibility may arise due to pinning of domain walls by crystal defects and imperfections in the crystals. A small remanent striction amounting to $\sim 1.6 \times 10^{-6}$, at $T = 2$ K, is indeed observed in our data (see Supplemental Material, Fig. S1 [49]), which indicates the presence of predominately mobile domain walls [52] in $NiTiO_3$.

Unlike uniaxial antiferromagnets, which show an abrupt magnetization jump at the spin-flop transition as, e.g., observed in $MnTiO_3$ [64], the magnetization in $NiTiO_3$ follows a sickle-shaped field dependence in the nonflopped phase, and the reorientation transition is associated with smooth right bending in M vs B (see Fig. 7). Such characteristic smooth nonlinear variation of magnetization in low fields is a manifestation of the multidomain state where spin reorientation takes place gradually by displacement of domain walls [56]. This is described [62] by

$$M = \left(\frac{1}{2}\right)\chi_e B\left[1 + \left(\frac{B}{B_d}\right)^2\right], \quad (4)$$

where χ_e is the high-field magnetic susceptibility. A linear fit to the M vs B curve [22] at $B > 4$ T yields $\chi_e = 0.06$ μ_B/f.u. T, which is represented by the solid blue line in Fig. 7. Using B_d from the analysis of the magnetostriction data (see Table IV) enables us to deduce the field dependence of M. The simulation using Eq. (4) is shown by the dashed line in Fig. 7. It yields a good description of the field-driven evolution of the magnetization in the multidomain state, thereby further confirming the applied phenomenological model. The blue line in Fig. 7 represents the expected magnetization in a single-domain easy-plane AFM with no in-plane anisotropy.

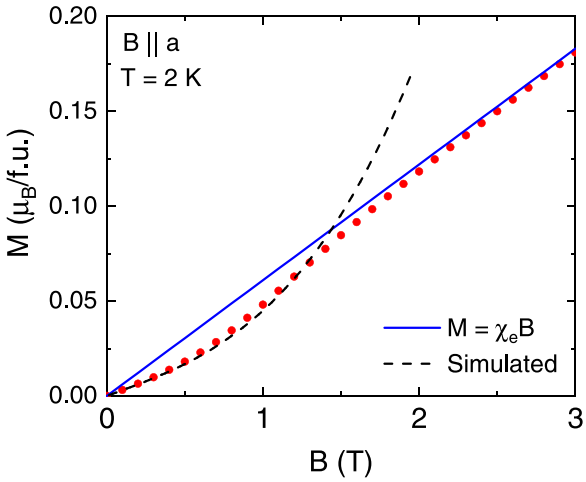

FIG. 7. Magnetization M, at $T = 2$ K, vs applied magnetic field $B||a$ axis. The solid blue line represents a linear fit to M in the high-field region, and the dashed black line shows a simulation to M at low fields (see the text for more details).

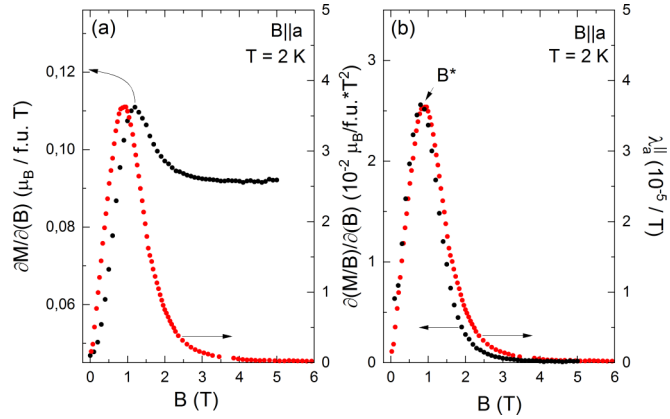

FIG. 8. (a) Scaling of $\partial M/\partial B$, (b) $\partial(M/B)/\partial B$ and $\lambda_a^{\parallel}$ versus B at $T = 2$ K.

The field-driven disappearance of the multidomain state yields different behavior of the magnetic susceptibility $\partial M/\partial B$ and the magnetostriction $\partial L/\partial B$. This is demonstrated in Fig. 8(a), where the derivative of the magnetization and the longitudinal magnetostriction coefficient $\lambda_a^{\parallel} = (1/L_a)\partial L_a/\partial(\mu_0 H)$ are shown at $T = 2$ K as a function of B. The data are scaled to match the corresponding peak values. According to the Ehrenfest relation

$$\frac{\partial B^*}{\partial p_i} = V_m \frac{\Delta\lambda_i}{\Delta[\partial M/\partial(\mu_0 H)]}. \quad (5)$$

Using molar volume $V_m = 42.01$ cm^3/mol and $B^* = 0.8$ T [Fig. 8(b)], we obtain the normalized pressure dependency $(1/B^*)\partial B^*/\partial p = 0.8$ kbar^{-1}. Positive magnetostriction in the monodomain phase reveals that [see also Fig. 5(a)] for each domain, the in-plane distortion in magnetic field is such that the lattice expands perpendicular to the spin direction. Hence, applying a uniaxial pressure p will induce an anisotropy in plane favoring domains with spins nearly parallel to p in the multidomain phase.

The scaling of $\partial(M/H)/\partial(\mu_0 H)$ and $\lambda_a^{\parallel}$ at 2 K in Fig. 8(b) shows that the quantities vary proportional to each other in the multidomain state peaking at B^*. The proportional variation $d(m/H)/dH \sim \lambda_a^{\parallel}$ is consistent on combining Eq. (3) with Eq. (4) and is a manifestation of the magnetoelastic nature of the domains. The behavior is expected from phenomenolog-

ical theories of magnetoelastic domains which describe the variation of magnetization and length changes by means of a single domain co-alignment parameter and its variation with magnetic field [61].

Apart from a large magnetocrystalline anisotropy which dictates the easy-plane spin structure in $NiTiO_3$, an additional small in-plane anisotropy may arise due to frozen strains in the domain walls [65]. The origin of this in-plane gap in the spin-wave spectrum of easy-plane antiferromagnets have been theoretically predicted [66,67] and experimentally observed in several easy-plane-type antiferromagnets, for example, the dihalides NiCl2 (∼0.3 T) and CoCl2 (∼0.8 T) by means of low-frequency resonance experiments [68]. Interestingly, $CoTiO_3$, which exhibits similar crystallographic and magnetic structure to $NiTiO_3$, shows an in-plane gap of ∼1 meV in recent inelastic neutron scattering experiments [24,25]. A frustrated bond anisotropic exchange interaction pinning the order parameters to the crystal axes [24,25] was suggested as the responsible mechanism for small in-plane gap in $CoTiO_3$, which is unlikely for $NiTiO_3$. However, in view of the theoretical predictions and experimental observations listed above, we speculate a small in-plane anisotropy to be present in $NiTiO_3$ corresponding with the frozen strains in magnetoelastic domain walls.

V. SUMMARY

In summary, we have studied in detail the magnetostructural coupling in magnetodielectric $NiTiO_3$ by means of single-crystal neutron diffraction and high-resolution dilatometry. Zero-field neutron diffraction confirms the multidomain A-type spin AFM ordering with preservation of crystallographic R-3 symmetry down to 2 K. Zero-field thermal expansion measurements reveal spontaneous lattice deformation at T_N. The dielectric permittivity ϵ scales with the square of the magnetic order parameter L in line with predictions of Landau theory, hence indicating finite magnetodielectric coupling in $NiTiO_3$. Our analysis suggests the presence of spin-phonon coupling as a responsible mechanism for the dielectric anomaly at T_N in $NiTiO_3$. In-field neutron diffraction shows the evolution of magnetic domains with spins perpendicular to the applied field. The effect of magnetic domains on magnetostriction has been discussed in light of phenomenological multidomain theories. We see magnetization and magnetostriction scale with each other in the multidomain state, revealing strong coupling of spins to the lattice.

ACKNOWLEDGMENTS

The work in this paper was performed in the frame of the International Max-Planck School IMPRS-QD. We acknowledge support by BMBF via the project SpinFun (13XP5088) and by Deutsche Forschungsgemeinschaft (DFG) under Germany's Excellence Strategy EXC2181/1-390900948 (the Heidelberg STRUCTURES Excellence Cluster) and through Project No. KL 1824/13-1.

[1] R. Zhong, T. Gao, N. P. Ong, and R. J. Cava, Sci. Adv. **6**, eaay6953 (2020).
[2] H. Liu and G. Khaliullin, Phys. Rev. B **97**, 014407 (2018).
[3] S. S. Pershoguba, S. Banerjee, J. C. Lashley, J. Park, H. Ågren, G. Aeppli, and A. V. Balatsky, Phys. Rev. X **8**, 011010 (2018).
[4] L. Chen, J.-H. Chung, B. Gao, T. Chen, M. B. Stone, A. I. Kolesnikov, Q. Huang, and P. Dai, Phys. Rev. X **8**, 041028 (2018).
[5] T. Matsumoto and S. Hayami, Phys. Rev. B **101**, 224419 (2020).
[6] A. I. Kurbakov, A. N. Korshunov, S. Y. Podchezertsev, A. L. Malyshev, M. A. Evstigneeva, F. Damay, J. Park, C. Koo, R. Klingeler, E. A. Zvereva, and V. B. Nalbandyan, Phys. Rev. B **96**, 024417 (2017).
[7] A. Nakua and J. Greedan, J. Solid State Chem. **118**, 402 (1995).
[8] C. Koo, E. A. Zvereva, I. L. Shukaev, M. Richter, M. I. Stratan, A. N. Vasiliev, V. B. Nalbandyan, and R. Klingeler, J. Phys. Soc. Jpn. **85**, 084702 (2016).
[9] K. S. Burch, D. Mandrus, and J.-G. Park, Nature **563**, 47 (2018).
[10] A. Maignan and C. Martin, Phys. Rev. Materials **2**, 091401(R) (2018).
[11] J. Werner, W. Hergett, M. Gertig, J. Park, C. Koo, and R. Klingeler, Phys. Rev. B **95**, 214414 (2017).
[12] N. D. Khanh, N. Abe, K. Matsuura, H. Sagayama, Y. Tokunaga, and T. Arima, Appl. Phys. L **114**, 102905 (2019).
[13] J. B. Goodenough and J. J. Stickler, Phys. Rev. **164**, 768 (1967).
[14] G. Shirane, S. Pickart, and Y. Ishikawa, J. Phys. Soc. Jpn. **14**, 1352 (1959).
[15] R. E. Newnham, J. H. Fang, and R. P. Santoro, Acta Crystallogr. **17**, 240 (1964).
[16] J. J. Stickler, S. Kern, A. Wold, and G. S. Heller, Phys. Rev. **164**, 765 (1967).
[17] G. S. Heller, J. J. Stickler, S. Kern, and A. Wold, J. Appl. Phys. **34**, 1033 (1963).
[18] J. Akimitsu, Y. Ishikawa, and Y. Endoh, Solid State Commun. **8**, 87 (1970).
[19] N. Mufti, G. R. Blake, M. Mostovoy, S. Riyadi, A. A. Nugroho, and T. T. M. Palstra, Phys. Rev. B **83**, 104416 (2011).
[20] M. Charilaou, D. Sheptyakov, J. F. Löffler, and A. U. Gehring, Phys. Rev. B **86**, 024439 (2012).
[21] J. K. Harada, L. Balhorn, J. Hazi, M. C. Kemei, and R. Seshadri, Phys. Rev. B **93**, 104404 (2016).
[22] K. Dey, S. Sauerland, J. Werner, Y. Skourski, M. Abdel-Hafiez, R. Bag, S. Singh, and R. Klingeler, Phys. Rev. B **101**, 195122 (2020).
[23] R. M. Dubrovin, N. V. Siverin, M. A. Prosnikov, V. A. Chernyshev, N. N. Novikova, P. C. M. Christianen, A. M. Balbashov, and R. Pisarev, J. Alloys Compd. **858**, 157633 (2020).
[24] B. Yuan, I. Khait, G.-J. Shu, F. C. Chou, M. B. Stone, J. P. Clancy, A. Paramekanti, and Y.-J. Kim, Phys. Rev. X **10**, 011062 (2020).

[25] M. Elliot, P. A. McClarty, D. Prabhakaran, R. D. Johnson, H. C. Walker, P. Manuel, and R. Coldea, arXiv:2007.04199 (2020).

[26] H. Watanabe, H. Yamauchi, and H. Takei, J. Magn. Magn. Mat. **15–18**, 549 (1980).

[27] R. Küchler, T. Bauer, M. Brando, and F. Steglich, Rev. Sci. Instruments **83**, 095102 (2012).

[28] T. Barth and E. Posnjak, Z. Kristallogr. **88**, 271 (1934).

[29] K. Kabsch, in *International Tables for Crystallography, Vol. F*, edited by M. G. Rossmann and E. Arnold (Kluwer Academic Publishers, Dordrecht, 2001), Chap. 11.3.

[30] *CrysAlisPro*, Agilent Technologies UK Ltd., Oxford (2011).

[31] R. H. Blessing, Acta Cryst. A **51**, 33 (1995).

[32] *SCALE3 ABSPACK, CrysAlisPro*, Agilent Technologies UK Ltd., Oxford (2011).

[33] W. R. Busing and A. Levy, Acta Cryst. **10**, 180 (1957).

[34] G. M. Sheldrick, *SHELXT*, University of Göttingen and Bruker AXS Gmbh, Karlshruhe, Germany (2012–2018).

[35] M. Ruf and B. C. Noll, *Application Note SC-XRD 503*, Bruker AXS Gmbh, Karlshruhe, Germany (2014).

[36] G. Sheldrick, Acta Cryst. A **71**, 3 (2015).

[37] G. M. Sheldrick, *SHELXL-20xx*, University of Göttingen and Bruker AXS Gmbh, Karlshruhe, Germany (2012–2018).

[38] W. Robinson and G. M. Sheldrick, *Crystallographic Computing 4* (IUCr and Oxford University Press, Oxford, UK, 1988).

[39] G. Sheldrick, Acta Cryst. A **64**, 112 (2008).

[40] G. Sheldrick, Acta Cryst. C **71**, 3 (2015).

[41] P. J. Brown, A. G. Fox, H.-C. Hu, J. I. Langford, H. Lipson, E. N. Maslen, M. A. O'Keefe, T. M. Sabine, and B. T. M. Willis, in *International Tables for Crystallography, Vol. C*, edited by E. Prince (Kluwer Academic Publishers, Dordrecht, 2004), 3rd ed., Chap. 6.

[42] P. Azavant and A. Lichanot, Acta Cryst. A **49**, 91 (1993).

[43] S. L. Morelhão, *Computer Simulation Tools for X-ray Analysis* (Springer International Publishing Cham, Switzerland, 2016), Chap. 1.3.1 and Appendix B, http://xraybook.if.usp.br.

[44] A. C. Larson, *Crystallographic Computing* (Munksgaard, Copenhagen, Denmark, 1970).

[45] CSD 2062660 (model A), 2062661 (model B), and 2062662 (model C) contain the supplementary crystallographic data for this paper. These data can be obtained from the Cambridge Crystallographic Data Centre's and FIZ Karlsruhe's joint Access Service via, https://www.ccdc.cam.ac.uk/structures/?

[46] G. Lawes, A. P. Ramirez, C. M. Varma, and M. A. Subramanian, Phys. Rev. Lett. **91**, 257208 (2003).

[47] T. D. Sparks, M. C. Kemei, P. T. Barton, R. Seshadri, E.-D. Mun, and V. S. Zapf, Phys. Rev. B **89**, 024405 (2014).

[48] U. Adem, G. Nénert, Arramel, N. Mufti, G. R. Blake, and T. T. M. Palstra, Eur. Phys. J. B **71**, 393 (2009).

[49] See Supplemental Material at http://link.aps.org/supplemental/10.1103/PhysRevB.103.134438 for up and down sweeps of relative length changes vs magnetic field in the ab-plane and crystal structure of $NiTiO_3$ in the ab-plane at 100 K and 2 K, respectively.

[50] M. K. Wilkinson, J. W. Cable, E. O. Wollan, and W. C. Koehler, Phys. Rev. **113**, 497 (1959).

[51] W. Knafo, C. Meingast, K. Grube, S. Drobnik, P. Popovich, P. Schweiss, P. Adelmann, T. Wolf, and H. v. Löhneysen, Phys. Rev. Lett. **99**, 137206 (2007).

[52] E. V. Gomonaj and V. M. Loktev, Low Temp. Phys. **25**, 520 (1999).

[53] H. Gomonay and V. M. Loktev, J. Phys.: Condens. Matter **14**, 3959 (2002).

[54] Y. Shapira and N. F. Oliveira, Phys. Rev. B **18**, 1425 (1978).

[55] M. Safa and B. Tanner, Phil. Mag. B **37**, 739 (1978).

[56] B. Tanner, Contemp. Phys. **20**, 187 (1979).

[57] T. Yamada, S. Saito, and Y. Shimomura, J. Phys. Soc. Jpn. **21**, 672 (1966).

[58] V. M. Kalita, A. F. Lozenko, and S. M. Ryabchenko, Low Temp. Phys. **26**, 489 (2000).

[59] V. M. Kalita, A. F. Lozenko, and P. A. Trotsenko, Low Temp. Phys. **28**, 263 (2002).

[60] V. M. Kalita and A. F. Lozenko, Low Temp. Phys. **27**, 645 (2001).

[61] V. M. Kalita, A. F. Lozenko, P. A. Trotsenko, and T. M. Yatkevich, Low Temp. Phys. **30**, 27 (2004).

[62] V. M. Kalita, A. F. Lozenko, S. M. Ryabchenko, and P. A. Trotsenko, Low Temp. Phys. **31**, 794 (2005).

[63] M. E. Lines, Phys. Rev. **131**, 546 (1963).

[64] H. Yamaguchi, H. Hiroyoshi, M. Yamada, H. Watanabe, and H. Takei, J. Mag. Magn. Mat. **31–34**, 1071 (1983).

[65] N. B. Weber, H. Ohldag, H. Gomonaj, and F. U. Hillebrecht, Phys. Rev. Lett. **91**, 237205 (2003).

[66] Y. B. Gaididei and V. Loktev, Solid State Commun. **39**, 1077 (1981).

[67] V. G. Bar'yakhtar, M. A. Savchenko, and V. Tarasenko, J. Exp. The. Phys. **22**, 1115 (1966).

[68] A. F. Lozenko and S. M. Ryabchenko, Sov. J. Exp. Theor. Phys. **38**, 538 (1974).